Partially graphitic hierarchical porous carbon nanofiber for high performance supercapacitors and lithium ion batteries

Jing Hu [a], Zhenglong Xu [a], Xiaoyan Li [a], Shijing Liang [a], Yuming Chen [a], Linlong Lyu [a], Haimin Yao [a], Zhouguang Lu [b, *], Limin Zhou [a, *]

[a] Department of Mechanical Engineering, The Hong Kong Polytechnic University, Hong Kong

[b] Department of Materials Science and Engineering, Southern University of Science and Technology, Shenzhen 518055, P. R. China.

Abstract

Partially graphitic hierarchical porous carbon nanofiber is prepared via electrospinning, pyrolysis, activation and acid treatment of the nascent fiber. The ameliorating structural features of the as-obtained carbon nanofiber, such as a relatively high graphitic degree, a high specific surface area and a large pore volume with hierarchical porous structure, acted synergistically, resulting in excellent electrochemical properties. When applied in supercapacitors, the obtained sample delivers a high specific capacitance of 287 F g^{-1} at 0.5 A g^{-1}, a high rate capacitance of 196 F g^{-1} at 100 A g^{-1} and a high capacity retention of 95.4 % at 5 A g^{-1} after 10000 cycles. When used as an anode for lithium ion batteries, the prepared electrodes display an exceptionally high reversible capacity of 1495 mAh g^{-1} at 0.1 A g^{-1}, superior cycle stability and an outstanding high-rate capacity of 391 mAh g^{-1} at 10 A g^{-1} for 1100 cycles. These values demonstrate the superiority of partially graphitic hierarchical porous carbon nanofiber as bi-functional electrodes in supercapacitors and Li-ion batteries with outstanding performance.

* Corresponding author. E-mail address: mmlmzhou@polyu.edu.hk (L. Zhou), luzg@sustech.edu.cn (G. Lu).

1. Introduction

The increasing demand to reduce fossil fuel consumption, address environmental issues and resolve potential energy crises has stimulated great interest in renewable and sustainable energy sources. Multiple energy harvesting technologies exist for renewable energy generation, including solar, wind, and geothermal based production. All of these technologies, however, rely heavily on the performance of energy storage systems [1-5]. Among energy storage systems, supercapacitors (SCs) and lithium ion batteries (LIBs) constitute two of the most dominant rechargeable energy storage device technologies currently on the market, owing to their superior performance. Despite this market dominance, the practical energy storage applications of SCs and LIBs are still far from satisfactory, and cannot meet the demand to power portable electronics, (hybrid) electric vehicles, energy-efficient industrial equipment and multiple energy harvesting technologies [6-11]. As the performance of SCs and LIBs essentially depends on the electrode materials they contain, the development of novel electrode materials with high power/energy density, high capacity and good cycling stability is urgently required to satisfy the demands placed on these important renewable energy technologies[12-14].

Nanoporous carbon materials, especially porous carbon nanofibers (CNFs) have stimulated tremendous attention in the area of energy storage due to their excellent chemical and physical stability, high surface areas, high aspect ratio, benign environmental characteristics and availability [15, 16]. Despite these numerous advantages, conventional porous CNFs struggle to simultaneously achieve high capacities

and excellent rate performances. For SCs, the porous texture characteristics of tortuosity, connectivity, pore size distribution, pore shape and graphitic degree have been proposed to affect electrode performance[17]. Several studies have further suggested that micropores (<2 nm) accommodate charge and strengthen capacitance, whereas mesopores (2-50 nm) and macropores (>50 nm) accelerate the diffusion speed of ions in electrodes and thereby improve power density[18, 19]. The lithium ion storage mechanism for carbonaceous materials can be divided into five types: intercalation in graphite carbon layers, covalent interaction, storage in 3D defects such as nanopores and cavities, storage at interfacial and heteroatom doping sites [20-22]. Thus, LIB capacity can be improved by boosting lattice disordering, fabricating pore spaces and increasing surfaces areas. These enhancements, however, also lead to kinetic problems, which are related to the speed of ion transport between inner pores and to electron transfer within electrodes. Given the link between increasing lattice disorder and kinetic problems, a significant remaining challenge facing this technology is the development of methods to rationally design the pore size and graphitic degree of carbon materials in ways that can shorten ion-diffusion paths and ensure excellent electrolyte permeability without sacrificing fast electron transport and high ion storage capacities.

Electrospinning is a powerful and versatile technique used to fabricate continuous CNFs, and which allows the structure and properties of the product to be controlled during fabrication via adjustments to processing conditions [23]. The porous structure of the CNF is typically generated by the addition of pore-templating agents (e.g. Ni, Sn, SiO_2), sacrificial polymers (e.g. PMMA, PS) and/or by chemical (e.g. KOH, $ZnCl_2$) and

physical (e.g. H_2O, CO_2) activations [24-27]. Although significant advances have been made in the application of these techniques, the successful synthesis of hierarchical porous carbon with optimal pore sizes, interconnected macro and microporous windows and controllable graphitic degree, remains an issue.

This study reports the successful fabrication of a partially graphitic CNF with hierarchical porous architectures via a sequence of electrospinning, calcination, activation and acid treatment. The partially graphitic CNFs assembled by this approach were further successfully utilized as bi-functional electrodes in SCs and LIBs. To the best of our knowledge, our work is the first reported example of introducing a combination of $MgCO_3$ and Ni as both the sacrificial component and the graphitization catalyst during the fabrication of graphitic cross-linked hierarchical porous CNFs. The novel structures reported herein were shown to possess the following advantages: (1) their one-dimensional structures shorten the diffusion distance of ions in the radial direction; (2) their high graphitic degree enhances the kinetics of ion and electron transport within electrodes; and (3) their hierarchical porous structure, which contains interconnected micro, meso and macropores, functions as the active site for ion adsorption, as an ion transport path and as an ion reservoir, simultaneously. Benefiting from these ameliorating structural features, the as-obtained material was found to exhibit good electrolyte accessibility, outstanding electrical conductivity and abundant reactive sites. The combination of these factors was seen to result in high capacitance, remarkable rate capability and superior cycle stability for SCs and LIBs that contained the novel CNFs reported here.

2. Experimental

2.1 Materials preparation

Magnesium chloride hexahydrate ($MgCl_2 \cdot 6H_2O$), sodium carbonate (Na_2CO_3), nitric acid (HNO_3) and dimethylformamide (DMF) were commercially sourced from International Laboratory, USA. Potassium hydroxide (KOH) and nickel(II) acetate tetrahydrate ($Ni(CH_3CO_2)_2 \cdot 4H_2O$) were purchased from Advanced Technology & Industrial Co., Hong Kong. Ethanol (EtOH) and polyacrylonitrile (PAN) were purchased from Sigma-Aldrich. All commercially sourced chemicals were analytical grade and were used without further purification.

Synthesis of $MgCO_3 \cdot 3H_2O$

200 mL of a 0.25 M aqueous solution of Na_2CO_3 was added slowly to 200 mL of a 0.25 M aqueous solution of $MgCl_2$ with vigorously stirring. After 1 h, the precipitate was collected by filtration and washed with deionized H_2O, followed by EtOH to completely remove residual Na and Cl ions. The white powder obtained in this way was dried at 60 °C for 6 h to yield $MgCO_3 \cdot 3H_2O$.

Preparation of MNP-CNF

1 g of $MgCO_3 \cdot 3H_2O$ and 0.2 g of $Ni(CH_3CO_2)_2 \cdot 4H_2O$ were added to 10 mL of DMF and subjected to sonication for 2 h. 1.9 g of PAN was dissolved in 10 mL of DMF at 70 °C with continuous stirring for 1 h. The suspension containing $MgCO_3$ and $Ni(CH_3CO_2)_2$ was then added to the PAN solution and stirred vigorously for 3 h. For electrospinning, the suspension obtained in this way was subsequently taken into a 20 mL plastic syringe with a stainless-steel needle connected to a high-voltage supply. The feeding rate was maintained at ~1 mL h^{-1}. The distance between the needle and the

aluminum foil collector was fixed at 20 cm and a high voltage of 17 kV was applied in between. The electrospinning process was conducted at room temperature in air. The $MgCO_3$/$Ni(CH_3CO_2)_2$/PAN neat nanofibers thus obtained were annealed in air at 250 °C for 2 h to ensure stabilization. Subsequently, the fibers were carbonized at 800 °C for 3 h under an atmosphere of N_2 and with a ramp rate of 5 °C min^{-1}, yielding the MgO/Ni/carbon nanofibers. A mixture of the freshly prepared MgO/Ni/CNF and KOH (w/w, 5:1) was then heated in a zirconium oxide crucible at 750 °C for 1 h under an N_2 atmosphere with a ramp rate of 5 °C min^{-1}. Finally, the product was treated with dilute HNO_3 to remove Ni and MgO, before being filtered and washed with deionized H_2O until the filtrate was measured as neutral. After drying at 60 °C for 6 h, the desired MNP-CNF product was obtained (M refers to $MgCO_3$, N refers to $Ni(CH_3CO_2)_2$ and P refers to PAN). As control samples, MP-CNF (containing 1 g $MgCO_3$, 1.9 g PAN and 20 mL DMF as precursors) and P-CNF (containing 1.9 g PAN and 20 ml DMF as precursors) were produced in the same way.

2.2 Material characterization

   he structures of fabricated samples were investigated by X-ray diffraction (XRD, Rigaku SmartLab with Cu Ka radiation (λ=0.154 nm) and confocal micro Raman spectrometer (Renishawn in Via Reflex). The N_2 adsorption/desorption isotherms were determined at 77K using an ASAP2020M apparatus (Micromeritics Instrument Corp., USA). Brunauer-Emmett-Teller (BET) and Barrett-Joyner-Halenda (BJH) models were used to calculate the specific surface area, pore volume and pore size distribution of the CNFs, respectively. Fiber morphologies were investigated via transmission electron microscopy (TEM; JEOL-2010F).

2.3 Electrochemical measurement

For SCs, a conventional three-electrode system containing a 6 M aqueous KOH solution as the electrolyte was used to evaluate electrochemical properties. A platinum foil and an Hg/HgO electrode were used as the counter and the reference electrode, respectively. The working electrodes were prepared by mixing the porous CNFs (80% w/w), carbon black (10% w/w), and PVDF (10% w/w) on a Ni foam. Cyclic voltammetry (CV) and electrochemical impedance spectroscopy (EIS) were conducted on a CHI 660C electrochemical workstation. CV testing was performed at voltages ranging from −0.9 to −0.1 V (*vs*. Hg/HgO) with scan rates varying from 5 to 200 mV s^{-1}. EIS spectra were measured with a constant amplitude of 5 mV at frequencies ranging from 100 kHz to 10 MHz. Galvanostatic charge-discharge (GCD) measurements were performed using a Neware CT-4008 supercapacitor testing system with a voltage window of −0.9 to −0.1 V (*vs*. Hg/HgO) and current densities ranging from (1 to 100 A g^{-1}).

To assess the application of the novel CNFs to LIBs, electrochemical measurements were conducted using 2032 coin cells with lithium metal foil as a counter electrode. The working electrode was composed of active materials, carbon black, and polyvinylidene fluoride at a weight ratio of 8:1:1. The components were stirred in *N*-methylpyrrolidone until a uniform mixture was obtained, before being cast on a copper foil. A 1 M solution of lithium hexafluorophosphate in a 1:1 v/v mixture of ethylene carbonate (EC) and diethyl carbonate (DEC) was used as the electrolyte. Celgard 2400 film was used as the separator film. The cell was assembled in a glovebox under an atmosphere of Ar. Galvanostatic charge-discharge (GCD) cycles were carried out using the LAND CT2001A battery test system at current densities ranging from 0.1 to 10 A g^{-1} and 0.01 to

3.0 V. The CV measurements were conducted on a CHI 660C electrochemical workstation with a scan rate of 0.1 mV s^{-1} (0–3.0 V). The EIS spectra were obtained using a constant voltage mode and a constant amplitude of 5.0 mV over frequencies ranging from 100 kHz to 0.01 Hz.

3. Results and discussion

The MNP-CNF fabrication process is illustrated in Scheme 1. A precursor solution containing $MgCO_3$, $Ni(CH_3CO_2)_2$ and PAN was used to electrospin the neat nanofibers. The fibers were then calcinated under an N_2 atmosphere, during which time $MgCO_3$ particles gradually decomposed releasing H_2O and CO_2 and resulting in porous MgO being obtained at around 500 °C. In subsequent decompositions of small molecules (such as CO, CO_2, CH_4 and C_2H_2) derived from the decomposition of PAN at higher temperatures [28], the void in the MgO network was deposited with carbon to form few-layer graphene [29, 30].

At the same time, the decomposition of PAN led to the formation of partially graphitic carbon as a result of the catalytic effect of Ni, which was present as a consequence of the decomposition of $Ni(CH_3CO_2)_2$. The MgO/Ni/CNF obtained in this way was further chemically activated with KOH, which caused micropores and defects to form, as well as a small quantity of graphitic tunnels via Ni particle diffusion. The desired, partially graphitic hierarchical porous carbon nanofibers were finally obtained after treatment with diluted HNO_3 to remove residual Ni and MgO.
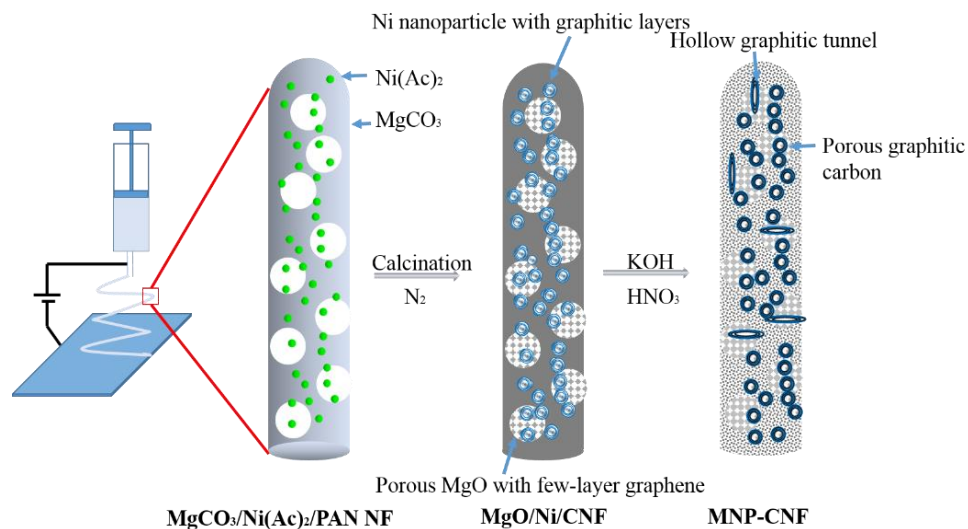
Scheme.1 Schematic illustration of the formation procedure for the MNP-CNF

XRD patterns reveal the structure of the MgO/Ni/CNF and the MNP-CNF. As shown in Fig. 1a, the diffraction peaks at $2\theta = 42.9^o$ and 62.3^o refer to a periclase MgO phase (JCPDS 45-0946), and the diffraction peaks at $2\theta = 44.5^o$, 51.8^o and 76.4^o can be well indexed to the Ni (JCPDS 04-0850), which illustrate the $MgCO_3$ and $Ni(Ac)_2$ were completely decomposed into MgO and Ni during the calcination process. The strong characterized diffraction peak at $2\theta = 26^o$ and weak reflection peak at $2\theta = 43^o$ index to the graphitic framework (JCPDS 41-1487). Furthermore, there are no characteristic peaks responding for MgO and Ni in MNP-CNF XRD pattern, which implies that the MgO and Ni are entirely removed by the action of HNO_3.

The Raman spectrum is employed to investigate the graphitic degree of the samples, as shown in Fig. 1 b. Two major peaks centered at 1346 and 1585 cm^{-1} are assigned to the D and G bands of carbon, respectively. The D band corresponds to disordered carbon or defects while the G band is a characteristic of graphitic structure. The I_D/I_G ratio has been previously used as an indicator of the graphitic degree of carbon materials, with higher

value suggesting a higher disorder degree within the sample [31, 32]. The I_D/I_G values of MNP-CNF, MP-CNF and P- CNF were estimated to be 0.84, 0.88,
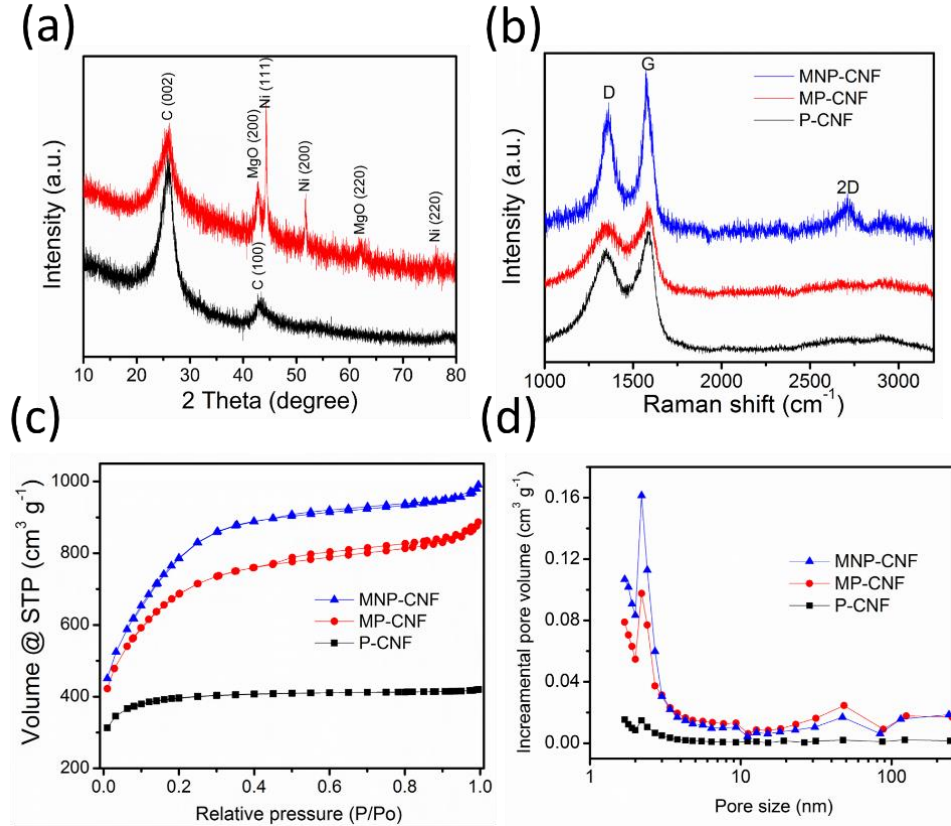

Fig. 1 (a) XRD patterns of MgO/Ni/ CNF and MNP-CNF, (b) Raman spectra, (c) Nitrogen adsorption-desorption isotherms and (d) the pore size distributions based on BJH model of MNP-CNF, MP-CNF, and P-CNF

and 0.91, respectively. This suggests that the graphitic degree of the porous carbon fiber was improved by MgO templating and Ni catalysis, and that the catalytic effect of Ni is stronger than that of MgO. Notably, signature 2D peak for graphene layers is observable at ~2,700 cm^{-1} for the MNP-CNF sample but no signal is detected for the MP-CNF sample, validating the presence of the few-layer graphene, which might be arising from the synergistic catalytic effect of MgO and Ni [33].

Table 1 Porous characteristics of the obtained samples

Sample	MNP-CNF	MP-CNF	P-CNF
BET surface area ($m^2 g^{-1}$)	2720	2285	1228
Total pore volume ($cm^3 g^{-1}$)	1.53	1.37	0.65
Average pore diameter (nm)	2.25	2.40	2.13

To further determine the porous structure of as-obtained samples, the N_2 adsorption-desorption isotherms were performed as shown in Fig. 1c. The specific surface area and porous structural parameters obtained for these samples are listed in Table 1. The MNP-CNF and the MP-CNF both display a hybrid I/IV type adsorption-desorption isotherm with steep N_2 adsorption at low relative pressure (< 0.4), a hysteresis at relative pressure between 0.4 and 1.0 and a slightly steep adsorption at the relative pressure ranging from 0.9-1.0, indicating the co-existence of micro-, meso- and macropores in the two samples[34, 35]. In contrast, the P-CNF shows a typical type-I microporous structure. The pore sizes distribution (PSD) based on BJH model are shown in Fig. 1d. For MNP-CNF, the pore size is centered at 2.2 nm, and is accompanied by a broad peak at 50 nm, further confirming the hierarchical porous structure with which micropores were incorporated into the walls of well-defined mesopores and marcopores in the fibers. The MP-CNF shows similar PSD plot to MNP-CNF. However, the peaks in the MNP-CNF plot at 2.2 nm and 50 nm is higher and lower, respectively, than that of MP-CNF. This suggests that the introduction of $MgCO_3$ played an important role in the formation mesopores and macropores, and that $Ni(CH_3CO_2)_2$ was the primary cause of mesopore formation. The P-CNF possesses mesopores centered at 2.2 nm and massive micropores, which were mainly induced as a result of KOH activation. Remarkably, the incremental

pore volume of the micropores and mesopores within MNP-CNF is larger than that of the other two samples, indicating that the presence of MgO and Ni potentially enhanced the chemical activation effect. In sharp contrast, the BET surface area of MNP-CNF is as high as 2721 m^2 g^{-1} while the surface areas of the MP-CNF and P-CNF are 2285 and 1228 m^2 g^{-1}, respectively. The ultra-high surface area contained in the MNP-CNF offers abundant reactive sites for energy storage, and its hierarchical structure enables facile ionic transports; these factors work in synergy, resulting in the excellent rate performance that was observed

The TEM image of the MNP-CNF prior to activation and acid treatment is reported in Fig. 2a. It shows a nanofiber structure with a diameter of ~ 450 nm, and the Ni and MgO particles are uniformly encapsulated in the carbon nanofiber framework. The spot- and ring-like patterns in selected area electron diffraction (SAED) (inset of Fig. 2a) verify the existence of Ni and MgO. The high-resolution TEM (HRTEM) images further confirm that the CNF consists of MgO and Ni crystalline particles with average layer spacing of approximately 0.21 and 0.176 nm, corresponding to the (200) plane of MgO and the (200) plane of Ni, respectively. TEM images of MNP-CNF in Fig. 2b show the diameter of the nanofiber is ~ 420 nm, which become smaller after activation and acid treatment. These values indicate that KOH activation and acid treatment etched the carbon structure. Large quantities of nanopores and few-layered graphene can be clearly observed in Fig. 2c. The micro-mesopores may be produced by KOH activation, the mesopores generated by removing Ni particles and MgO template, and the connected macropores may mainly come from etching off porous MgO particles. From the HRTEM image of MNP-CNF illustrates in Fig. 2d, it is obviously observed that nanopores and tunnels with few

graphitic carbon layers were distributed throughout the amorphous carbon nanofiber. The typical (002), (100) and (122) ring features in the inset SAED pattern indicate graphitized character, which is consistent with the XRD and Raman results. The P-CNF shows a uniform diameter (~200 nm) with obvious porous structure on the surface (Fig. S1a). The diameter variation effected by viscosity changing of the precursors. The HRTEM image of P-CNF (Fig. S1b) indicates a low graphitic degree. The MP-CNF has some embedded porous structure which left by removing MgO particles (Fig. S1c). Few-layer graphene was also observed in the HRTEM image of MP-CNF (Fig. S1d), indicating that the $MgCO_3 \cdot 3H_2O$ template may also catalyze the formation of graphene layers.
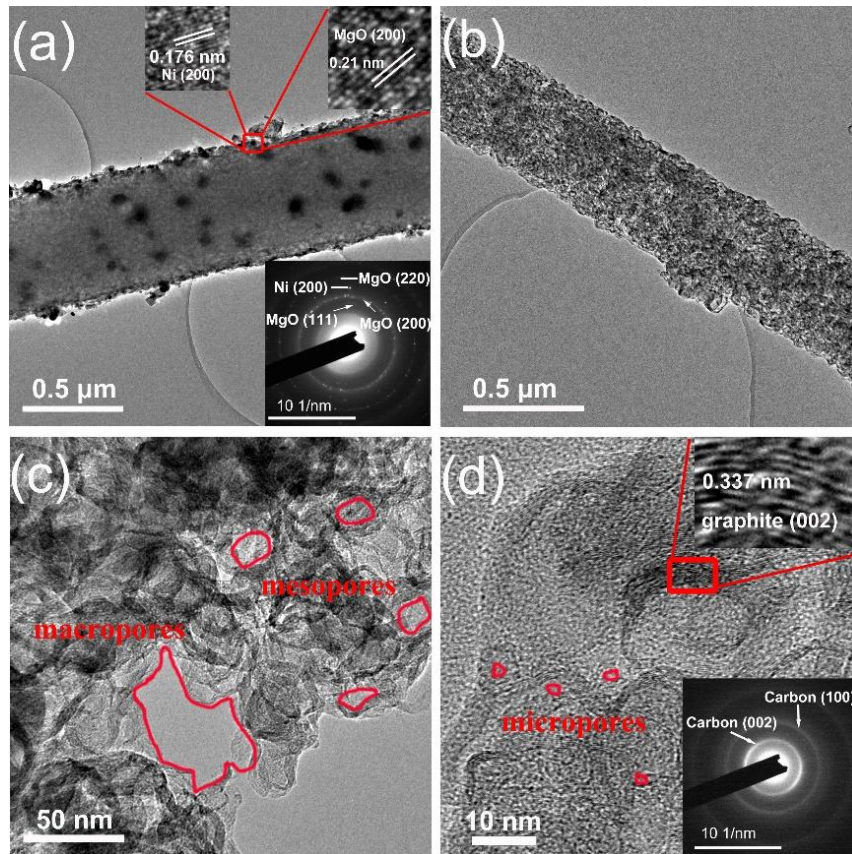

Fig. 2 (a) TEM, HRTEM and SAED pattern image of MgO/Ni/MNP-CNF, (b) and (c) TEM images of MNP-CNF, (d) HRTEM and SAED pattern image of MNP-CNF

The electrochemical performances of the MNP-CNF in SCs was investigated in 6 M KOH aqueous electrolyte in a three-electrode system. Fig. 3a displays the CV curves of MNP-CNF at different scan rates ranging from 5 to 200 mV s^{-1}, which retain a nearly perfect rectangular shape even at a high scan rate of 200 mV s^{-1}. Furthermore, the responsive current density increased with scan rate enhancement, indicating an ideal electric double- layer capacitor (EDLC) behavior and the good capacitive performance of quick charge-discharge. Fig. 3b exhibits the GCD curves at various current densities from 2 to 100 A g^{-1} in the potential window from -0.1 to -0.9 (*vs*. Hg/HgO). GCD curves of
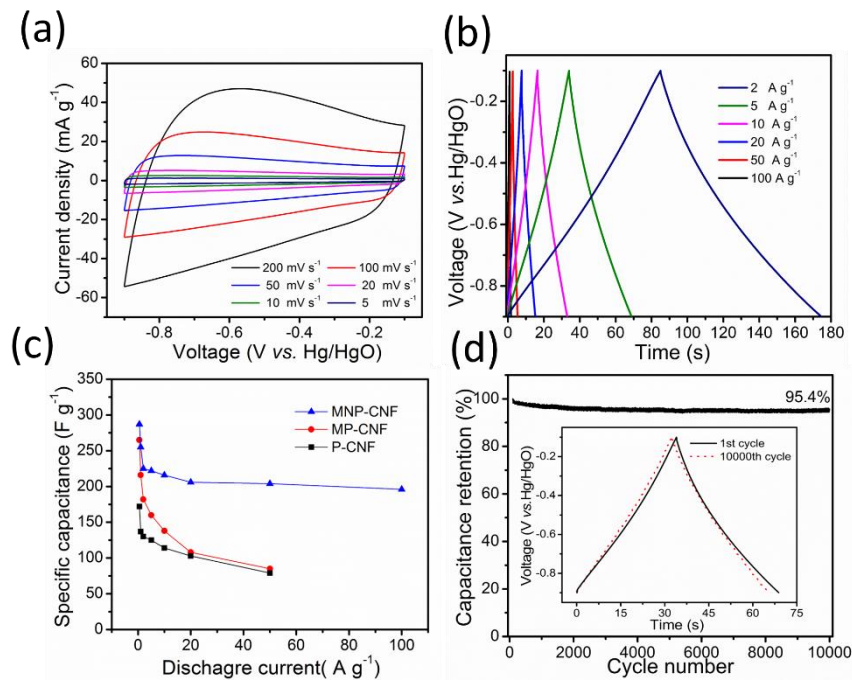

Fig. 3 (a) Cyclic voltammetry curves of MNP-CNF at different scan rates. (b) The galvanostatic charge-discharge curves of MNP-CNF at different current densities. (c) The variation of specific capacitances with current densities for MNP-CNF, MP-CNF, and P-CNF. (d) Cycling performance of MNP-CNF at current density of 5A g^{-1}, the inset shows the galvanostatic charge-discharge curves of the 1st and 10000th cycles.

MNP-CNF, MP-CNF and P-CNF at 0.5 and 1 A g^{-1} are shown in Fig. S2a. These curves show typical triangular shape and with no obvious ohmic drop, further confirming the

highly capacitive nature of the fabricated materials. The GCD curves of MNP-CNF, MP-CNF and P-CNF were seen to suffer from various degrees of ohmic potential drop accompany with the increasing of current (Table S1), the degree of ohmic potential drop at a given current density is arranged in a descending order according to the series: P-CNF>MP-CNF> MNP-CNF, which reflects the MNP-CNF possesses the lowest internal resistance. The specific capacitance of electrode was calculated using the equation $C= I \times \Delta t / (\Delta V \times m)$, where C (F g^{-1}) is the specific capacitance, I (A) indicates the discharge current, Δt (s) represents the discharge time, ΔV (V) designates the voltage change excluding the voltage drop (IR drop) during the discharge process, and m (g) means the mass of the active material in the electrode[36]. The results calculated using this equation are shown in Fig. 3c. As can be seen, the specific capacitance of MNP-CNF is 287 F g^{-1} at the current density of 0.5A g^{-1}. Notably, the MNP-CNF exhibits a high rate capacitance of 196 F g^{-1} when the current density increases to 100 A g^{-1}. As is also shown in Fig. 3c, the specific capacitance of MNP-CNF is much higher than that of MP-CNF and P-CNF at same current densities, as the former, benefits from abundant energy storage sites and high electrical conductivity. The P-CNF delivers the fastest capacity degradation among the three electrodes, which is mainly caused by its poor electronic conductivity. The cycle performance of MNP-CNF is shown in Fig. 3d. The MNP-CNF electrodes retained 95.4 % of the initial capacitance after 10000 cycles at a current density of 5 A g^{-1}, which suggests a good electrochemical cycling behavior and excellent reversibility of MNP-CNF. In addition to this, the inset image in Fig. 3d displays a typical triangular charge-discharge curve of the 1st and the 10000th cycle, indicating an excellent stability.

Noticeably, the performance of the MNP-CNF for SCs is distinguished when compared to most of carbon-based materials (in Table 2).

Table 2. Comparison of the electrochemical performance of carbon-based materials in SCs.

| Materials	electrolyte	C_m (F g^{-1})	Current density	Cycling stability (%)	Ref.
N-doped hierarchical porous carbon	6 M KOH	271, 114	0.2, 40 (A g^{-1})	94.1, 10k cycles	[37]
N-rich porous carbon nanofiber	6 M KOH	202, 164	1, 30	97, 3k cycles	[38]
Ordered mesoporous carbon/graphene aerogel	6 M KOH	197, 141	0.5, 10	92.6, 1k cycles	[39]
N-doped hollow mesoporous carbon nanosphere	5 M KOH	214, 165	2, 40	97, 5k cycles	[40]
N-doped carbon@graphitic carbon	1 M H$_2$SO$_4$	270, 173	2, 10	100, 10k cycles	[41]
MNP-CNF	6 M KOH	287, 196	0.5, 100	95.4, 10k cycles	This work
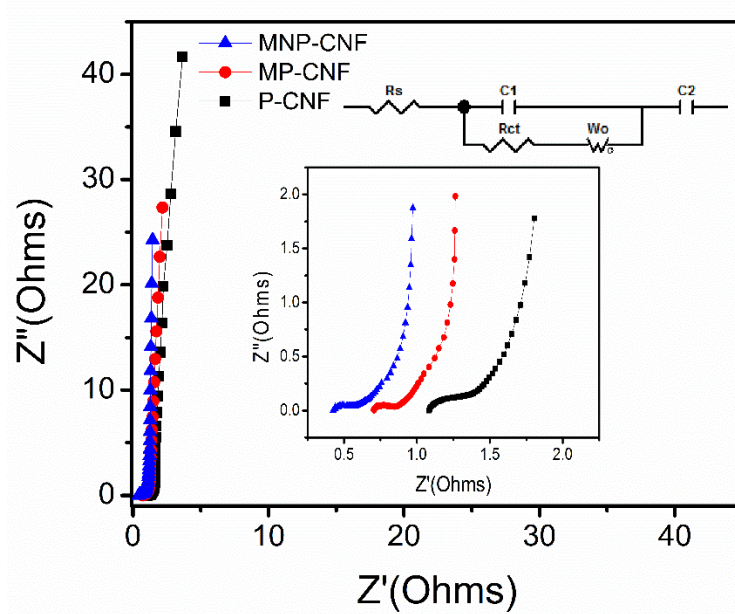
Fig. 4 Nyquist plots of the MNP-CNF, MP-CNF, and P-CNF electrodes in 6 M KOH. The inset shows the zoom-in part of the high frequency region

To further understand the capacitive behavior of MNP-CNF, MP-CNF and P-CNF, EIS test was investigated over a frequency range from 10 kHz to 10 MHz at open circuit voltage. As shown in Fig. 4，the Nyquist plot of as-obtained samples with a semicircle in the high frequency domain and a linear tail in the low frequency region displays similar

pattern to plots obtained from carbonaceous materials reported previously[42-44]. Herein, the high-frequency intersection with the X axis indicates the electrochemical system resistance (Rs) including the intrinsic resistance of electroactive material and electrolyte, and the interface resistance, the diameter of the semicircle represents the charge transfer resistance (Rct) of on the electrode/electrolyte interface, the linear tail reflects Warburg resistance (Zw) related to the diffusion behavior of electrolyte to the electrode surface[45, 46]. The values of Rs and Rct are calculated by using Zview software according to the equivalent circuit model (inset of Fig. 4). The Rs of MNP-CNF, MP-CNF and P-CNF is ~0.44, 0.72 and 1.08 Ω, respectively. Furthermore, the Rct of MNP-CNF is smaller than the control samples. The lower Rs and Rct indicate a well-connected interface nature of electrolyte ions and electrode and good intrinsic electronic properties of the material[47]. The hierarchical nanoporous architecture increases the pore accessibility, and the highly graphitic structure with few-layer graphene enhance the ion transfer speed. The high slope at low frequency indicates the MNP-CNF electrode has a pronounced capacitor behavior[48]. The better conductivity of MNP-CNF is beneficial to the enhancement of electrochemical performance.

The MNP-CNF was further investigated as an anode material for LIBs. The electrochemical performance is shown in Fig. 5. Fig. 5a shows a typical CV curves of the porous carbon anode in the first three cycles between 0.0 and 3.0 V (*vs*. Li/Li$^+$) at a scan rate of 0.1 mV s^{-1}. Notably, the first cathodic sweep is different from the subsequent CV curves. For the first sweep, it can be observed a cathodic peak located at ~1.43 V which is disappeared during the following cycles and a stronger intensity of peak located at ~0.6V compared with the intensity during the following cycles, which is usually

attributed to some side reactions associated with the decomposition of electrolyte on the electrode surfaces and interfaces formation of solid-electrolyte interphase (SEI) film, and the loss of some irreversible reactive sites, corresponding to the capacity loss during the first cycle[49-51]. Remarkably, the CV curves are almost overlapped after the initial cycle, indicating the stable and superior reversibility of the MNP-CNF. Fig. 5b displays initial two GCD profiles of MNP-CNF at a current density of 0.1 A g^{-1} in a voltage range of 0.01-3.0 V, which is similar to other carbonaceous materials [27, 34].There are obvious slopes in the potential range of 0.9-1.75 V and 0.3-0.9 V in the first cycle, which is in accordance with the cathodic peak located at ~1.43 V and broad peak located at ~0.6 V observed during CV scans. The initial discharge and charge capacitance of MNP-CNF is 2815 and 1495 mAh g^{-1}, respectively, with an initial Coulombic efficiency (CE) approximately 53.1%, the large capacity loss is usually attributed to irreversible formation of SEI, consistent with the CV results. The initial reversible specific capacity is four times more than the theoretical capacity of graphite (372 mAh g^{-1}), which is also superior to those of many other carbonaceous materials [52-58]. The high capacity of the MNP-CNF may be attributed to the high specific surface area and partially graphitic structure offer more lithium ion storage sites in addition to the conventional graphite intercalation mechanism. Lithium ions can be electrochemically adsorbed on and intercalated into both sides of the disordered carbon layer surface, as well as the micro/mesopores inside MNP-CNF, resulting in a higher reversible Li storage capacity. The cycling performance of MNP-CNF at current density of 0.1 and 10 A g^{-1} is shown in Fig. 5c and Fig. 5d, respectively. The reversible specific capacity remains ~ 1210 mAh g^{-1} after 110 cycles at 0.1 A g^{-1}. The initial reversible capacity of MNP-CNF at 10 A g^{-1} is

372 mAh g^{-1} followed by marginal decrease in the subsequent cycles and then gradually increases to a high reversible specific capacity of 391 mAh g^{-1} after 1100 cycles, which is much higher than the theoretical value of graphite. The increase in capacity with cycling can be attributed to the activating process of the electrode [50, 59]. Furthermore, the CE is rapidly increaseing from 29% in the first cycle to 97% in the tenth cycle and remains above 99% during the subsequent cycles, indicating the formation of stable SEI layers and good reversibility of the electrodes. The MNP-CNF electrode also displays good rate performance (Fig. 5e). The reversible specific capacities are 846, 670, 573, 461, 398 and 373 mAh g^{-1} at 1, 2, 4, 6, 8 and 10 A g^{-1}, respectively, which are much higher than that of MP-CNF and P-CNF. When the rate is turned back to 1 A g^{-1} after cycling at different current densities, the capacity can be recovered to 805 mAh g^{-1}, which shows very stable cycling performance. In order to further understand the reasons for superior electrochemical performance of the MNP-CNF for LIBs, EIS of obtained samples were carried out at fresh coin cell. The results are presented in Fig. 5f. The Nyquist plots obtained were modeled with an appropriate electric equivalent circuit (inset of Fig. 5f). Based on the equivalent circuit, the R_s value of the MNP-CNF, MP-CNF and P-CNF electrode is 11.44, 16.51 and 18.22 Ω, respectively, and the *Rct* value is 67.12, 114.2 and 143.5 Ω, respectively. As expected, the MNP-CNF delivers higher electrical conductivity and rapider charge-transfer reaction for lithium ion insertion and extraction, which indicates the superior pore size distribution and the higher degree of graphitic can effectively enhance the electrochemical conductivity of electrode materials.
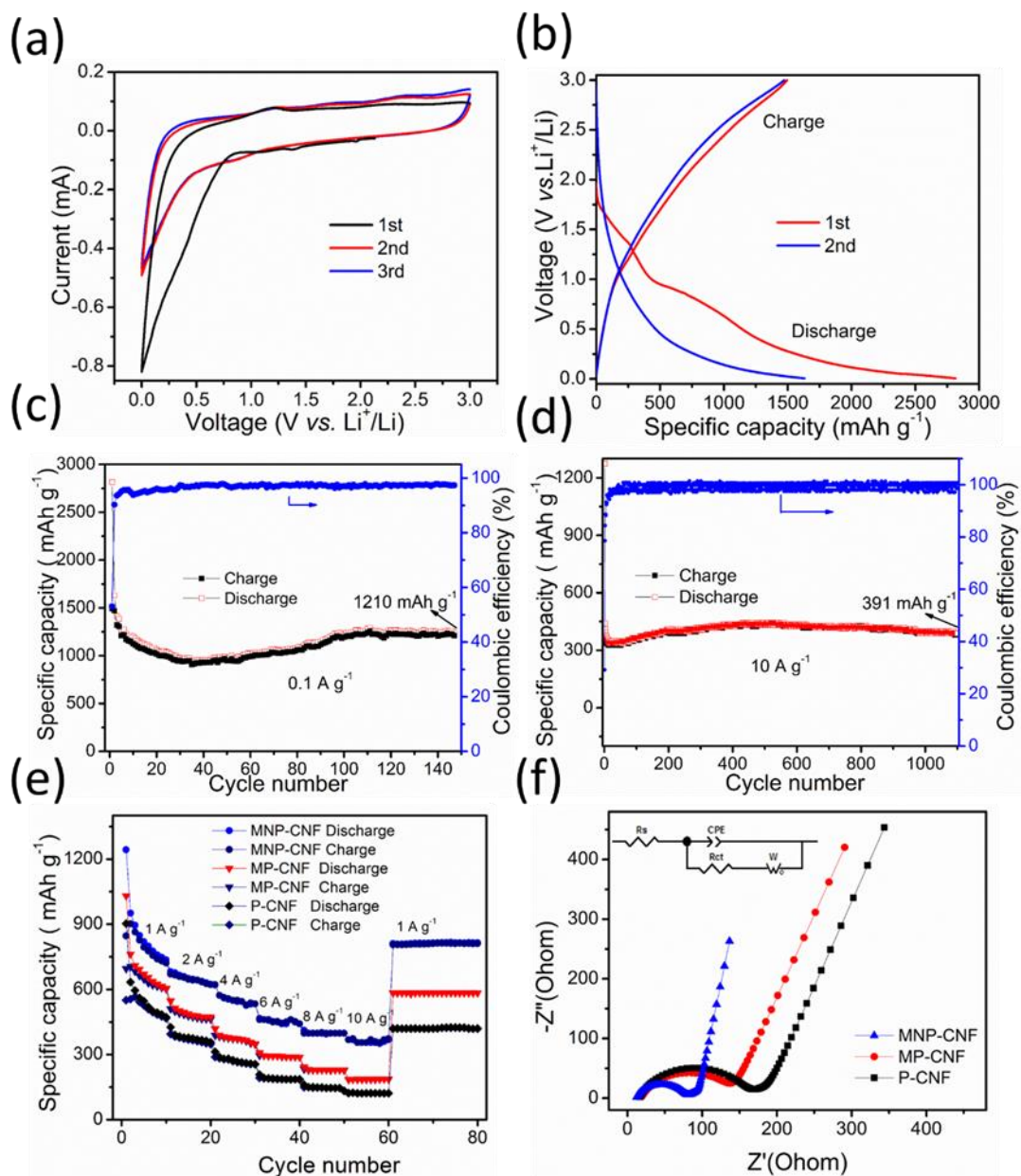
Fig. 5 Electrochemical performances of MNP-CNF: (a) cyclic voltammetry curves at a scan rate of 0.1 mV s^{-1}, (b) Galvanostatic charge-discharge curves at 0.1 A g^{-1}, (c) and (d) cycling performance at 0.1 A g^{-1} and 10 A g^{-1} respectively. (e) Capacities over cycling at different rates and (f) Nyquist plots of MNP-CNF, MP-CNF, and P-CNF.

4. Conclusion

In summary, a partially graphitic hierarchical porous carbon nanofiber (MNP-CNF) has been successfully fabricated using an electrospinning technique in which MgO and Ni served as the pore-templating agent and catalyst, respectively. The fabricated MNP-CNF shows a high graphitic degree and a high specific surface area (2721 m^2 g^{-1}) with hierarchical porosity (average pore diameter is 2.47 nm). These structural characteristics are seen to, synergistically contribute to the impressive electrochemical properties of the fabricated fiber. When used as SCs, this material exhibited impressive rate performance (196 F g^{-1} at 100 A g^{-1}) and excellent cycling life stability (4.6 % capacitance loss after 10000 cycles at 5 A g^{-1}). The fabricated material further shows reversible specific capasity (1495 mAh g^{-1}) that is superior to other porous carbon materials currently used as anode materials for LIBs. Our results indicate that the MNP-CNF is a promising candidate for the development of next generation energy storage. Moreover, with respect to the multiple synergistic effects of its unique structure, this material has potencical application in a variety of high-power energy storage devices.

Acknowledgement

Appendix A. Supplementary data

The following is the supplementary data related to this article:

References

[1] S. Chu, A. Majumdar, Nature, 488 (2012) 294-303.
[2] D. Bruce, K. Haresh, J.-M. Tarascon, Science, 334 (2011) 928-935.
[3] N. Armaroli, V. Balzani, Angew. Chem. Int. Ed., 46 (2007) 52-66.
[4] C. Liu, F. Li, L.P. Ma, H.M. Cheng, Adv. Mater., 22 (2010) E28-E62.

[5] J.L. Shi, D.D. Xiao, M. Ge, X. Yu, Y. Chu, X. Huang, X.D. Zhang, Y.X. Yin, X.Q. Yang, Y.G. Guo, Adv. Mater., 30 (2018) 1705575.

[6] S. Patrice, G. Yury, D. Bruce, Science, 343 (2014) 1210-1211.

[7] J.-M. Tarascon, M. Armand, Nature, 414 (2001) 359-367.

[8] X. Wang, G. Yushin, Energy Environ. Sci., 8 (2015) 1889-1904.

[9] D. Larcher, J.-M. Tarascon, Nat. Chem., 7 (2015) 19-29.

[10] R. Schmuch, R. Wagner, G. Hörpel, T. Placke, M. Winter, Nature Energy, 3 (2018) 267.

[11] M. Baro, Jaidev, S. Ramaprabhu, Appl. Surf. Sci., 503 (2020) 144069.

[12] R.N. Bulakhe, V.Q. Nguyen, D. Tuma, Y.R. Lee, H. Zhang, S. Zhang, J.-J. Shim, J. Ind. Eng. Chem., 66 (2018) 288-297.

[13] D.K. Nandi, S. Sahoo, S. Sinha, S. Yeo, H. Kim, R.N. Bulakhe, J. Heo, J.J. Shim, S.H. Kim, ACS Appl. Mater. Interfaces, 9 (2017) 40252-40264.

[14] R.N. Bulakhe, V.H. Nguyen, J.-J. Shim, New J. Chem., 41 (2017) 1473-1482.

[15] G.-H. An, H.-J. Ahn, Carbon, 65 (2013) 87-96.

[16] Y. Xu, C. Zhang, M. Zhou, Q. Fu, C. Zhao, M. Wu, Y. Lei, Nat. Commun., 9 (2018).

[17] J. Niu, R. Shao, M. Liu, J. Liang, Z. Zhang, M. Dou, Y. Huang, F. Wang, Energy Storage Mater., 12 (2018) 145-152.

[18] T. Yang, R. Zhou, D.-W. Wang, S.P. Jiang, Y. Yamauchi, S.Z. Qiao, M.J. Monteiro, J. Liu, Chem. Commun., 51 (2015) 2518-2521.

[19] M.E. Suss, T.F. Baumann, M.A. Worsley, K.A. Rose, T.F. Jaramillo, M. Stadermann, J.G. Santiago, J. Power Sources, 241 (2013) 266-273.

[20] N.A. Kaskhedikar, J. Maier, Adv. Mater., 21 (2009) 2664-2680.

[21] D. Pan, S. Wang, B. Zhao, M. Wu, H. Zhang, Y. Wang, Z. Jiao, Chem. Mater., 21 (2009) 3136-3142.

[22] J.R. Dahn, T. Zheng, Y.H. Liu, J.S. Xue, Science, 270 (1995) 590-593.

[23] H.-G. Wang, S. Yuan, D.-L. Ma, X.-B. Zhang, J.-M. Yan, Energy Environ. Sci., 8 (2015) 1660-1681.

[24] B. Zhang, F. Kang, J.-M. Tarascon, J.-K. Kim, Prog. Mater. Sci., 76 (2016) 319-380.

[25] J. Wang, S. Kaskel, J. Mater. Chem., 22 (2012) 23710-23725.

[26] C. Kim, Y.I. Jeong, B.T.N. Ngoc, K.S. Yang, M. Kojima, Y.A. Kim, M. Endo, J.W. Lee, Small, 3 (2007) 91-95.

[27] Y. Chen, X. Li, X. Zhou, H. Yao, H. Huang, Y.-W. Mai, L. Zhou, Energy Environ. Sci., 7 (2014) 2689-2696.

[28] X. Li, Y. Chen, H. Huang, Y.-W. Mai, L. Zhou, Energy Storage Mater., 5 (2016) 58-92.

[29] C. Cui, W. Qian, Y. Yu, C. Kong, B. Yu, L. Xiang, F. Wei, J. Am. Chem. Soc., 136 (2014) 2256-2259.

[30] M.S.A. Rahaman, A.F. Ismail, A. Mustafa, Polym. Degrad. Stabil., 92 (2007) 1421-1432.

[31] F. Zheng, Y. Yang, Q. Chen, Nat. Commun., 5 (2014).

[32] Y. Zhang, L. Chen, Y. Meng, J. Xie, Y. Guo, D. Xiao, J. Power Sources, 335 (2016) 20-30.

[33] R. Raccichini, A. Varzi, V.S.K. Chakravadhanula, C. Kübel, A. Balducci, S. Passerini, J. Power Sources, 281 (2015) 318-325.

[34] J. Hou, C. Cao, F. Idrees, X. Ma, ACS nano, 9 (2015) 2556-2564.

[35] Y.S. Yun, M.H. Park, S.J. Hong, M.E. Lee, Y.W. Park, H.-J. Jin, ACS Appl. Mater. Interfaces, 7 (2015) 3684-3690.

[36] L. Qie, W. Chen, H. Xu, X. Xiong, Y. Jiang, F. Zou, X. Hu, Y. Xin, Z. Zhang, Y. Huang, Energy Environ. Sci., 6 (2013) 2497-2504.

[37] J. Zhou, Z. Zhang, W. Xing, J. Yu, G. Han, W. Si, S. Zhuo, Electrochim. Acta, 153 (2015) 68-75.

[38] L.-F. Chen, X.-D. Zhang, H.-W. Liang, M. Kong, Q.-F. Guan, P. Chen, Z.-Y. Wu, S.-H. Yu, ACS nano, 6 (2012) 7092-7102.

[39] R. Liu, L. Wan, S. Liu, L. Pan, D. Wu, D. Zhao, Adv. Funct. Mater., 25 (2015) 526-533.

[40] C. Liu, J. Wang, J. Li, M. Zeng, R. Luo, J. Shen, X. Sun, W. Han, L. Wang, ACS Appl. Mater. Interfaces, 8 (2016) 7194-7204.

[41] J. Tang, R.R. Salunkhe, J. Liu, N.L. Torad, M. Imura, S. Furukawa, Y. Yamauchi, J. Am. Chem. Soc., 137 (2015) 1572-1580.

[42] Y.S. Yun, S. Lee, N.R. Kim, M. Kang, C. Leal, K.-Y. Park, K. Kang, H.-J. Jin, J. Power Sources, 313 (2016) 142-151.

[43] J. Jiang, J. Zhu, W. Ai, Z. Fan, X. Shen, C. Zou, J. Liu, H. Zhang, T. Yu, Energy Environ. Sci., 7 (2014) 2670-2679.

[44] S. Shanmugapriya, S. Surendran, Y.S. Lee, R.K. Selvan, Appl. Surf. Sci., 492 (2019) 896-908.

[45] Z. Li, L. Zhang, B.S. Amirkhiz, X. Tan, Z. Xu, H. Wang, B.C. Olsen, C. Holt, D. Mitlin, Adv. Energy. Mater., 2 (2012) 431-437.

[46] J. Hou, C. Cao, F. Idrees, X. Ma, ACS nano, 9 (2015) 2556-2564.

[47] Y. Li, Z. Li, P.K. Shen, Adv. Mater., 25 (2013) 2474-2480.

[48] J. Gamby, P. Taberna, P. Simon, J. Fauvarque, M. Chesneau, J. Power Sources, 101 (2001) 109-116.

[49] X. Jia, G. Zhang, T. Wang, X. Zhu, F. Yang, Y. Li, Y. Lu, F. Wei, J. Mater. Chem. A, 3 (2015) 15738-15744.

[50] L. Qie, W.M. Chen, Z.H. Wang, Q.G. Shao, X. Li, L.X. Yuan, X.L. Hu, W.X. Zhang, Y.H. Huang, Adv. Mater., 24 (2012) 2047-2050.

[51] A. Wang, S. Kadam, H. Li, S. Shi, Y. Qi, npj Computational Materials, 4 (2018) 15.

[52] Z.-Y. Sui, C. Wang, Q.-S. Yang, K. Shu, Y.-W. Liu, B.-H. Han, G.G. Wallace, J. Mater. Chem. A, 3 (2015) 18229-18237.

[53] Y. Fang, Y. Lv, R. Che, H. Wu, X. Zhang, D. Gu, G. Zheng, D. Zhao, J. Am. Chem. Soc., 135 (2013) 1524-1530.

[54] L. Zhang, G. Xia, Z. Guo, D. Sun, X. Li, X. Yu, J. Power Sources, 324 (2016) 294-301.

[55] T. Hu, X. Sun, H. Sun, G. Xin, D. Shao, C. Liu, J. Lian, Phys. Chem. Chem. Phys., 16 (2014) 1060-1066.

[56] W. She, J. Wang, X. Zhang, M. Sun, C. Xie, J. Xiao, S. Wang, J. Power Sources, 401 (2018) 55-64.

[57] P. Sennu, N. Arun, S. Madhavi, V. Aravindan, Y.-S. Lee, J. Power Sources, 414 (2019) 96-102.

[58] C. Xu, D. Niu, N. Zheng, H. Yu, J. He, Y. Li, ACS Sustain. Chem. Eng., 6 (2018) 5999-6007.

[59] X. Huang, H. Yu, J. Chen, Z. Lu, R. Yazami, H.H. Hng, Adv. Mater., 26 (2014) 1296-1303.